

# Crustal shear wave velocity structure in the northeastern Tibet based on the Neighbourhood algorithm inversion of receiver functions

Zhenbo Wu,<sup>1</sup> Tao Xu,<sup>2,3</sup> Chuntao Liang,<sup>4</sup> Chenglong Wu<sup>2</sup> and Zhiqiang Liu<sup>1</sup>

<sup>1</sup>Chengdu University of Technology, College of Geophysics, Chengdu 610059, China

<sup>2</sup>State Key Laboratory of the Lithospheric Evolution, Institute of Geology and Geophysics, Chinese Academy of Sciences, Beijing 100029, China. E-mail: xutao@mail.iggcas.ac.cn

<sup>3</sup>CAS Center for Excellence in Tibetan Plateau Earth Sciences, Beijing 100101, China

<sup>4</sup>Chengdu University of Technology, State Key Laboratory of Geohazard Prevention and Geoenvironment Protection and Key Laboratory of Earth Exploration and Information Techniques of Sichuan Province, Chengdu 610059, China

Accepted 2017 December 7. Received 2017 November 29; in original form 2017 June 22

## SUMMARY

The northeastern (NE) Tibet records and represents the far-field deformation response of the collision between the Indian and Eurasian plates in the Cenozoic time. Over the past two decades, studies have revealed the existence of thickened crust in the NE Tibet, but the thickening mechanism is still in debate. We deployed a passive-source seismic profile with 22 temporary broad-band seismic stations in the NE Tibet to investigate the crustal shear wave velocity structure in this region. We selected 288 teleseismic events located in the west Pacific subduction zone near Japan with similar ray path to calculate *P*-wave receiver functions. Neighbourhood algorithm method is applied to invert the shear wave velocity beneath stations. The inversion result shows a low-velocity zone (LVZ) is roughly confined to the Songpan–Ganzi block and Kunlun mountains and extends to the southern margin of Gonghe basin. Considering the low *P*-wave velocity revealed by the wide-angle reflection–refraction seismic experiment and high ratio of  $V_p/V_s$  based on  $H-\kappa$  grid searching of the receiver functions in this profile, LVZ may be attributed to partial melting induced by temperature change. This observation appears to be consistent with the crustal ductile deformation in this region derived from other geophysical investigations.

**Key words:** Asia; Inverse theory; Crustal imaging; Crustal structure.

## 1 INTRODUCTION

Himalayan–Tibetan orogenic belt created by the collision between Indian–Eurasian plates in the Cenozoic has been paid much attention by many researchers on its tectonic history (e.g. Yin & Harrison 2000) and uplift deformation mechanism (e.g. Tapponnier & Molnar 1976; England & Houseman 1989; Royden *et al.* 1997). Although the general idea of its geodynamic deformation mechanism has been well accepted, many aspects still continue to challenge scientists. Regarding to the growth mechanisms of the Tibetan plateau, there are primarily three end-member models, that is, the rigid block extrusion, the thin-viscous-sheet continuous deformation model and the crustal channel flow model. Each of them can explain some geological phenomena but fail on others. The rigid block model shows materials in the plateau interior extruded to the east and southeast along the large-scale strike-slip faults, but fails to explain the distribution of north–south trending rifts in central plateau and relatively smooth velocity gradients of strain rate near those major faults observed by Global Positioning System (GPS) (Zhang *et al.* 2004). On the contrary, continuous deforma-

tion cannot interpret the existence of some major faults located in the boundaries between microblocks and on the edge of Tibetan Plateau. Although there have been geological and geophysical evidences to some extent supporting crustal channel flow model in the southeastern plateau (Yao *et al.*, 2008, 2010; Liu *et al.* 2014), but still no clear evidence observed in the northeast (Zhang *et al.* 2011; Liang *et al.* 2012; Li *et al.* 2014a,b; Xu *et al.* 2014; Shen *et al.* 2015).

According to geological studies (Meyer *et al.* 1998; Fang *et al.* 2007; Gan *et al.* 2007; Mulch & Chamberlain 2006; Clark *et al.* 2010), the northeastern (NE) Tibet is still in its young stage in extending northeastwardly and uplifting vertically. Recent GPS measurements (Gan *et al.* 2007) show that about 10 mm yr<sup>-1</sup> of NE–SW or NNE–SSW horizontal shortening is being accommodated in NE Tibet. Regional tectonic units (Fig. 1) have been initiated by a large-scale orogeny happened about 10 Ma in this section. Ancient Altyn Tagh fault became active again in the Eocene (Yin & Harrison 2000). Kunlun fault probably began left-lateral faulting at 10 ± 2 Ma (Fu & Awata 2007). Haiyuan fault began to activate in the late Miocene (Zheng *et al.* 2006). The initiation of dextral movement of

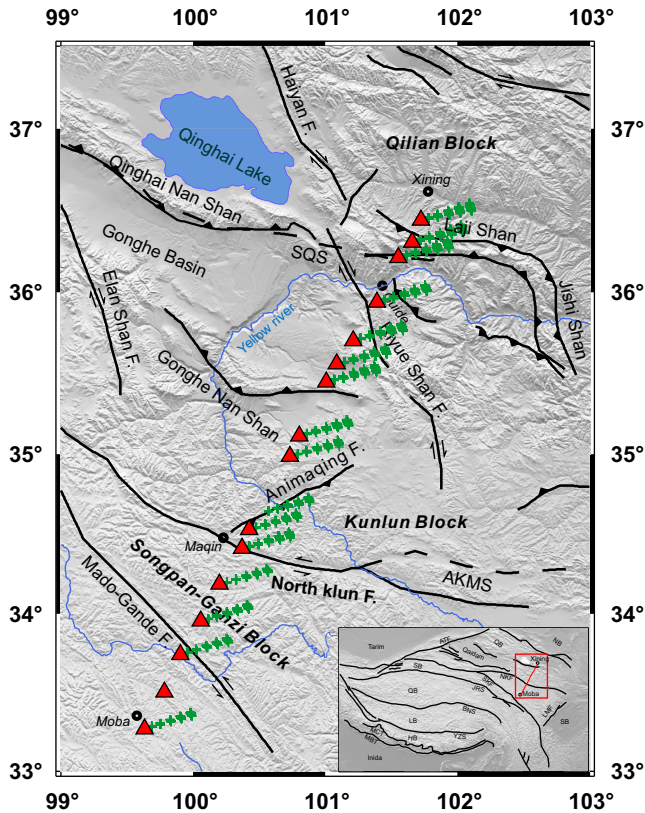


**Figure 1.** Tectonic map of the study region in NE Tibet shown with a red box in the lower right corner. Seismic experiment is deployed between the cities of Xining (to the north) and Moba (to the south); the red triangles represent temporary broad-band seismic stations. The green crosses represent the converted  $P$ -to- $S$  piercing points of receiver functions with Gaussian filter 2.0 at depth of 20, 40, 60, 80 and 100 km. Acronyms for sutures and faults: YZS, Indus-Zangbo suture; BNS, Bangong-Nujiang suture; JRS, Jinsha suture; AKMS, Animaqing-Kunlun-Muztagh suture; SQS, South Qilian suture; SKF, South Kunlun fault; NKF, North Kunlun fault; LMF, Longmen shan fault; ATF, Altyn Tagh fault; MCT, Main Central thrust; MBT, Main Boundary thrust; HB, Himalaya block; LB, Lhasa block; QB, Qiangtang block; SB, Songpan–Ganzi block; NB, North China and SB, Sichuan basin.

two north–northwest trending, Elasha and Riyue Shan faults, began in  $9$  or  $10 \pm 3$  Ma (Yuan *et al.* 2011). Cenozoic tectonic deformation in the Jishi Shan, Qilian Shan as well as their adjacent basins occurred near 8 Ma (Zhang *et al.* 2006). Laji Shan began an episodic rapid deformation and uplift since about 8 Ma (Fang *et al.* 2007). Therefore, the NE Tibet is an ideal experiment field for studying lateral outgrowth in the surrounding regions of the Tibetan Plateau, and far-field deformation response as Indian plate constantly moves northward and persistently collides with the Eurasian plate.

Over the past two decades, previous studies have revealed the existence of thickened crust in the NE Tibet, but the thickening mechanism is still in debate. For the active-source seismic surveys,  $P$  and  $S$  velocities provided by the wide-angle reflection–refraction experiment (Galvé *et al.* 2002) suggest that upper crust thickening only exist to the north of North Kunlun fault. However, another seismic refraction experiment (Liu *et al.* 2006) suggests that thickening happens mainly in the lower crust in the NE Tibet. On the other hand, the studies of passive-source seismic surveys also show conflict interpretations. The results of surface wave tomography based on ambient seismic noise and earthquake data (Yang *et al.* 2012; Karplus *et al.* 2013; Li *et al.* 2014a,b; Wei *et al.* 2017) show

low velocities are widely distributed in middle-to-lower crust of the Songpan–Ganzi block; and these results are interpreted to support the crustal flow model of Clark & Royden (2000). However, Low Poisson's ratios observed by receiver functions indicate the composition of the whole crust is more felsic in the NE Tibet and it may suggest that upper crust thickening may dominate the north–south shortening for the persistent collision of the Indian–Eurasian plates (Vergne *et al.* 2002; Pan & Niu 2011; Li *et al.* 2017a). Recently, the similar low Poisson's ratios are estimated by  $H$ - $\kappa$  grid searching of the receiver functions of a dense seismic array with 1317 stations in the NE Tibet (Wang *et al.* 2017).

In order to further probe this enigma, we conducted a passive-source seismic experiment in the NE Tibet. This profile has been already studied using the methods of common conversion point stacking and  $H$ - $\kappa$  grid searching of receiver functions (Xu *et al.* 2014), and joint inversion of surface wave dispersions and  $P$ -wave receiver functions to construct a crustal shear wave velocity structure beneath the profile (Deng *et al.* 2015; Wu *et al.* 2017). But the surface wave dispersions used in the joint inversion of Deng *et al.* (2015) were derived from a large-scale region with the grid resolution of  $0.5^\circ \times 0.5^\circ$  ( $\sim 55$  km). The authors also obtained the receiver functions from globally available teleseismic events. Due to varying backazimuths and ray paths of the events, their results are inevitably complicated by the propagating effects and lateral structure variations in the crust beneath the station. In contrast, we used the cross-correlation of ambient seismic noise between stations along the profile to extract surface wave dispersions with higher accuracy, and particularly we selected the teleseismic events with similar ray parameters to compute receiver functions. The joint-inversion method based on linear inversion theory and a damped least-squares scheme depends strongly on the initial model. Therefore, this paper uses a non-linear inversion method, that is, the Neighbourhood algorithm (NA), to reduce the dependence on the initial model. It is well known that the receiver functions are less sensitive to the absolute value of shear wave velocity than the velocity changes. We recalculate  $P$ -wave receiver functions with several low-pass Gaussian filters with different frequency band, then use NA to invert crustal shear wave velocity beneath the profile.

## 2 DATA AND METHOD

The passive-source seismic experiment between Xining and Moba (Fig. 1) in NE Tibet was conducted from 2010 November to 2011 June. 22 temporary broad-band seismic stations with Reftek-72A data loggers and Guralp CMG3-ESP sensors with bandwidths of 0.02–30 or 60 s were deployed. Average space interval between stations is about 10–15 km. Three-component ground movements are recorded with 40 samples per second at each station.

### 2.1 Receiver functions

Considering ambiguity arising from propagation effects along different ray paths and anisotropic effects from different azimuths, we only selected 288 teleseismic events to compute receiver functions. Rays from these events have similar backazimuths ( $70^\circ$ – $80^\circ$ ) and similar ray parameters ( $\sim 0.078$ ). All these events are located at the west Pacific subduction zone near Japan (Fig. 2). Time-domain iterative deconvolution (Ligorria & Ammon 1999) is applied to extract  $P$ -wave receiver functions with several different low-pass frequency Gaussian filters. The filter-width parameter  $a$  of Gaussian filter is 1.0, 1.5, 2.0 and 2.5 that respectively corresponds to high cut-off frequency of 0.5, 0.7, 1.0 and 1.2 Hz. It should be pointed out that

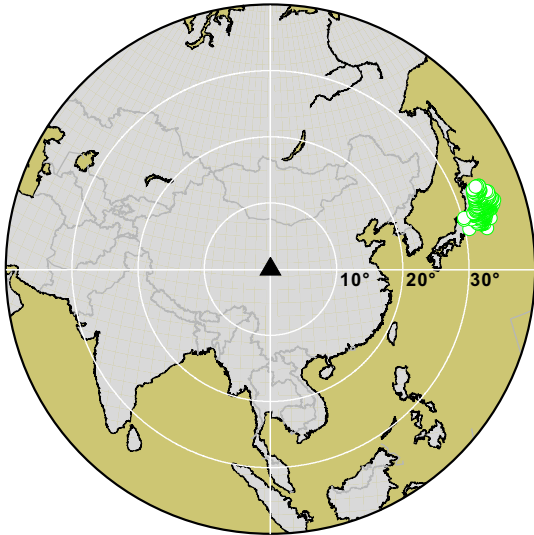


**Figure 2.** Global map showing the 288 selected teleseismic events (green circles) used to calculate receiver functions. These events are located roughly in the same area and have similar epicentral distances (around  $35^\circ$ ), backazimuths ( $70^\circ$ – $80^\circ$ ) and ray path. The black triangle indicates the approximate location of the profile.

S03, S09, S18 and S24 stations have very few or no good quality receiver functions for the selected teleseismic events (strictly limited in backazimuth and epicentral distance). As shown in Fig. 4(b), the amplitude of the results of station S15 seems to be abnormal compared to the others. Similar situation happens for S05 station. It is worth noting that station S15 and S05 locate in the vicinity of thrust Animaqing fault and the strike-slip Riyue Shan fault, respectively. The complicated geological conditions near these faults may result in the abnormal teleseismic recordings. Finally, only the receiver functions from 16 stations (shown in Fig. 1 with red triangles) are used to constrain the crustal velocity structure beneath the profile.

As you can see in Fig. 3,  $P$ -to- $S$  converted phases are clearly displayed at time window near 6–8 s in the receiver functions of station S06. Receiver functions vary with different Gaussian filters even though they are corresponding to the same crustal structure beneath the station S06. That reflects the gradually improved structure resolution from low to high frequency. As shown in Fig. 3, the results for parameter  $a = 1.0$  only show the  $PmS$  phase at time  $\sim 7.2$  s produced by the Moho, but there are two more converted phases at time  $\sim 1.7$  and  $\sim 3.75$  s in the results for parameter  $a = 2.0$  and 2.5. It is generally acknowledged that converted phases before  $PmS$  in a receiver function are probably produced by the velocity discontinuity within the crust. If we fit these four sets of receiver functions simultaneously using NA inversion, we should be able to find a model including both smooth large-scale regional tectonics and also high-resolution local crustal structure beneath the stations along the profile.

## 2.2 Phase-weighted stack

Shown as green crosses in Fig. 1, the  $PmS$  piercing points of ray paths at depth of 20, 40, 60, 80 and 100 km are aligned along the profile. It indicates that the shear wave velocity structure constrained by these receiver functions is capable of representing crustal structures beneath the profile. On the other hand, the piercing points of the rays from all events are almost overlapped for every station, which

indicates the receiver functions have similar traveltime for  $P$ -to- $S$  converted phases and allow us to stack them by a simple scheme to avoid time moveout stemmed from different epicentral distances between station and teleseismic events. If we use all global events to compute receiver functions, the differences of time moveout due to different ray parameters could be relatively large and produce artificial errors.

A technique called phase-weighted stack (PWS), which is based on the instantaneous phase and used to weight the samples of an ordinary, linear stack. It permits detection of coherent arrivals and mutes incoherent noise signal (Schimmel & Paulssen 1997). First, an analytic signal  $S(t)$  is constructed from the receiver function  $s(t)$ . This is done by ascribing the signal  $s(t)$  to the real part of the analytic signal and its Hilbert transform  $H(s(t))$  to the imaginary part of  $S(t)$  as follows:

$$S(t) = s(t) + iH(s(t)) = A(t) \exp[i\Phi(t)] \quad (1)$$

where  $A(t)$  is the envelope of  $S(t)$  and  $\Phi(t)$  is called instantaneous phase. Secondly, the PWS  $g(t)$  for all receiver functions of each station can be performed by:

$$g(t) = \frac{1}{N} \sum_{j=1}^N s_j(t) \left| \frac{1}{N} \sum_{k=1}^N \exp[i\Phi_k(t)] \right|^\nu \quad (2)$$

where  $N$  is the number of receiver functions used. The phase stack acts as a filter with a certain sharpness of the transition between phase similarity and dissimilarity, which is controlled by the power  $\nu$ . The linear stack is retrieved with  $\nu = 0$ . In this study,  $\nu$  is equal to 1. The PWS is a non-linear stack and involves waveform distortion. However, coherent signals will not be distorted too much since the instantaneous phase is presumed to be more or less stationary on the individual traces. The strongest distortions are expected for incoherent signals.

We apply PWS technique to stack all receiver functions at each station. Fig. 4(a) shows the comparison between PWS and linear stack of receiver functions for 16 stations. Subsequent incoherent signals after converted  $PmS$  phase have been suppressed to some extent without influencing useful coherent signals produced by intercrustal and Moho discontinuities. The advantage of PWS on high-frequency band is more notable than low-frequency band. In Fig. 4(b), it is obvious to see that the amplitude of station S15 is much smaller than other stations for all frequency bands. As mentioned before, the PWS results of 16 stations are used in the inversion of NA.

## 2.3 Neighbourhood algorithm

The inversion of receiver function is known to be a non-linear problem, where linearized inversion techniques suffer from a strong dependence on the initial model. This can be directly dealt with global minimization algorithm. The latter has been an efficient way of exploring a dimensionally large model parameter space and well suited for receiver function modeling with complex crustal structure. NA was developed by Sambridge (1999a,b) and has been used in different kinds of geophysical inversions (Sherrington & George 2004; Bannister *et al.* 2004; Hetényi *et al.* 2006; Snoko & Sambridge 2002). In the process, it self-adaptively produces some sample models from a multidimensional model parameter space with its sizes known. Then, synthetic receiver functions are calculated for each of these models, and cross-correlation between synthetics and observed data. Smaller regions of model parameter space containing low misfit models are searched iteratively in more detail to find a

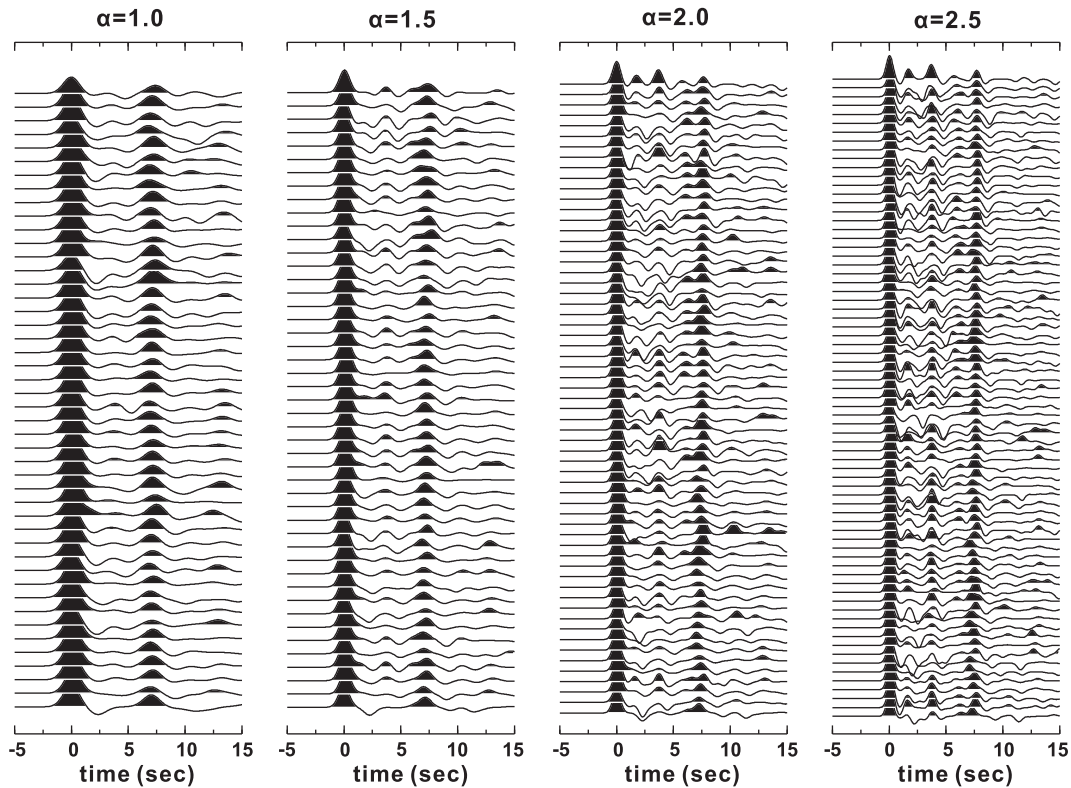


Figure 3. Four groups of receiver functions with different Gaussian parameters calculated by time-domain iterative deconvolution at station S06.

group ensemble of best-fitting models, rather than seeking a single optimal model.

Because the survey region includes Cenozoic intramontane basins such as Gonghe and Guide basins in Kunlun block and Xining basin in Qilian block, and Triassic turbidite sediments with thickness over 10 km in Songpan–Ganzi block (Enkelmann *et al.* 2007), the model parameter space used in the NA inversion includes a sedimentary layer and is shown in Table 1. The crustal structure of study region is parametrized using 24 parameters; four parameters representing the minimum and maximum values of  $S$ -wave velocities at the top and bottom of each layer, the layer thickness, and the ratio of  $V_p$  and  $V_s$  are assigned to describe the property of each of the six layers. The two shear wave velocities in each layer allow definition of a velocity gradient for that layer, which allows representation of a large number of potential velocity–depth distributions. Layers are assumed to be isotropic and flat, which means that structure beneath each seismic station is 1-D. In this study, velocity gradient is fixed in each layer which means velocity linearly increases with depth within the layer.

The NA requires only two user-defined parameters,  $n_r$  and  $n_s$ , to guide the search. As  $n_r$  and  $n_s$  are increased, it will be more explorative and as they are decreased it will be more exploitative. In each iteration,  $n_s$  samples are randomly generated from within the best  $n_r$  Voronoi cells by performing a uniform random walk which relaxes to a spatially uniform distribution within each cell. In a multidimensional model parameter space, as the number of samples increases, the space begins to saturate and the average number of natural neighbours tends to a constant (Sambridge 1998). Namely, for the algorithm to perform well, the initial sample size in the model parameter space should be big enough to achieve saturation of the Voronoi cells. In this study,  $n_r$  and  $n_s$  parameters are given after a number of trials. The inversion starts with 600 samples

from model space. In each iteration, resamples 200 models from 20 chosen models with the lowest misfit of all models generated so far (Sambridge 1999a,b). For each station, the inversion involves 500 iterations, generating 100 600 velocity models. The final result is represented by the mean value of an ensemble of 1000 best-fitting models. The synthetic receiver function based on the best-fitting model is calculated and compared with the observed data.

### 3 INVERSION RESULTS

The inversion result of NA method provides not only the shear wave velocity structure, but also the  $V_p/V_s$  ratio in the crust beneath the station. In order to evaluate the stability of the inversion result along the profile, first, receiver functions with different Gaussian parameters for each station are inverted individually. Then, all receiver functions with different Gaussian parameters for each station are inverted together using NA method.

#### 3.1 Inverted models and synthetics

Based on abovementioned model parameter space and inversion parameters, the NA method is applied to obtain the crustal velocity structure along the profile. In the first step, receiver functions with Gaussian parameter  $\alpha = 1.0, 1.5, 2.0$  and  $2.5$  for each station are inverted individually. In Fig. 5, four inversion results of station S16 are shown in the upper panels from left to right (Figs 5a–d), respectively. The corresponding observed and synthetic receiver functions are shown in the lower panel. The synthetics are based on the best-fitting model shown as red lines in the upper panel. For each frequency band (Gaussian filter), the figure contains defined model space (between two solid black lines), all gen-

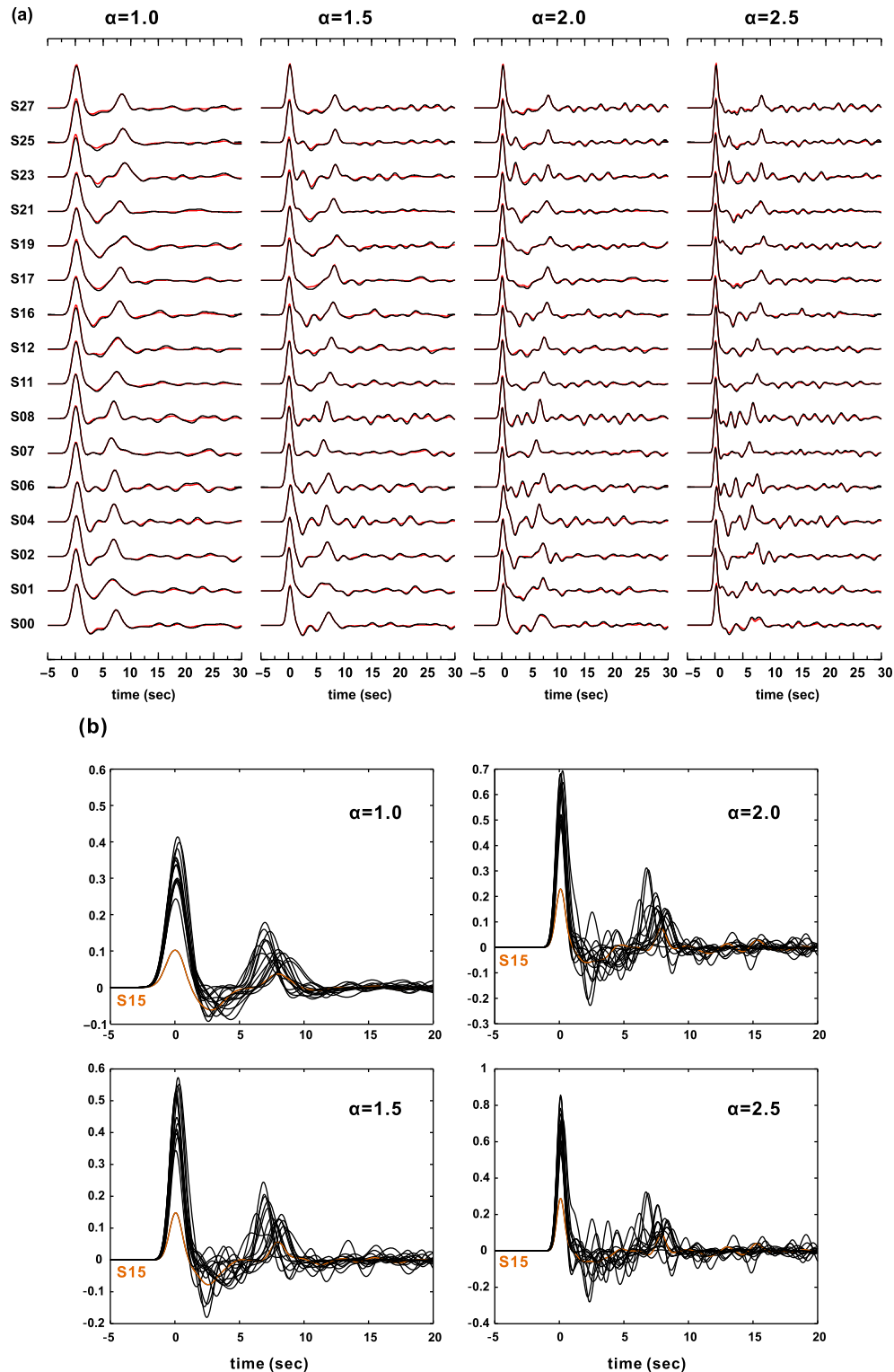


**Figure 4.** (a) The comparison between linear stacked (black line) and phase-weighted stacked (red line) receiver functions of 16 seismic stations. (b) Phase-weighted stacked receiver functions for 16 stations, and the yellow lines are the results of station S15, whose amplitude is much less than others.

erated models (grey lines), the best-fitting model (red line) and the average (blue line) of 1000 best-fitting models (shown in colour bar). As you can see, the model parameter space is almost completely covered by all generated models in the inversion process, while 1000 best-fitting models are confined in a narrow band. As shown in Fig. 5, although absolute shear wave velocity values base

on receiver functions with different filters, a stable character still emerges from the inversion results. A low-velocity zone (LVZ) exists constantly in the middle-to-lower crust beneath the station S16. The depth of LVZ in the model with Gaussian parameter  $\alpha = 1.0$  is shallower than that of the other three results. The reason is attributed to the lower resolution resulted from the lower frequency, and vice

**Table 1.** Parameter bound used in the NA inversion. Numbers in brackets are indices.

Layer	Thickness (km)	Upper_Vs (km s <sup>-1</sup> )	Lower_Vs (km s <sup>-1</sup> )	$V_p/V_s$
Sediment	0–3 (1)	1.5–3.0 (7)	1.5–3.0 (13)	2.0–3.0 (19)
Basement	2–5 (2)	1.7–3.2 (8)	1.7–3.2 (14)	1.65–2.0 (20)
Upper crust	5–20 (3)	2.0–3.5 (9)	2.4–4.0 (15)	1.65–2.0 (21)
Middle crust	5–20 (4)	2.5–4.0 (10)	2.8–4.5 (16)	1.7–2.0 (22)
Lower crust	10–25 (5)	3.0–4.5 (11)	3.0–4.5 (17)	1.7–2.0 (23)
Mantle	5–30 (6)	3.2–5.0 (12)	4.0–5.0 (18)	1.7–2.0 (24)

versa. Additionally, the NA inversion also provides the  $V_p/V_s$  ratio in the crust (cyan lines in Figs 5a–d). Both its absolute value and change trend of  $V_p/V_s$  are less well controlled than the shear wave velocities, although relatively high  $V_p/V_s$  values are correlated with LVZs.

In order to further evaluate the stability of the inversion result along the profile, we also fit four groups of receiver functions for each station simultaneously in the NA inversion. Two examples have been shown in Fig. 6. The upper left panel is the inversion result of station S12; the corresponding synthetic and observed waveforms are shown below. The right-hand panels are for station S19. As you can see, a LVZ exists in the middle-to-lower crust beneath the station S19, while the waveforms also contain one negative phase between the direct  $P$  wave and converted  $PmS$  phase. In contrast, the inversion result of station S12 has no obvious similar character. It should be noted that both stations S16 and S19 locate in the Songpan–Ganzi block. Their inversion results indicate that a low shear wave velocity

zone possibly exists in the middle-to-lower crust in that block. The rest of inversion results of 14 stations are shown in Fig. 7. Their corresponding waveforms are shown in Fig. 8. According to the traveltime of  $PmS$  phase based on these waveforms, it is known that the Moho depth is shallower from south to north along the profile.

### 3.2 2-D image of crustal velocity structure

2-D crustal shear wave velocity beneath the profile is shown in Figs 9 and 10(c). In Fig. 9, the inversion results of receiver functions with increasing frequency bands are shown from top to bottom. Although there are some local differences among four inversion results, a stable LVZ undoubtedly emerges in middle-to-lower crust beneath the Songpan–Ganzi block, if only considering the velocity changes without regard of the absolute velocity value. The top 2-D image is the crustal velocity structure corresponding to the Gaussian parameter  $\alpha = 1.0$ . It displays an LVZ in the shallower depth and relatively smooth horizontal change due to the low resolution corresponding to the low frequency band.

The inversion results derived from fitting all four receiver functions with different frequency bands for each station is displayed in Fig. 10(c). Similarly, a prominent LVZ stands out in the middle-to-lower crust beneath the Songpan–Ganzi block and northwards to the southern margin of Gonghe basin. The white crosses represent averaged crustal thickness beneath seismic stations based on H– $\kappa$  grid searching of the receiver functions (Xu *et al.* 2014).

### S16

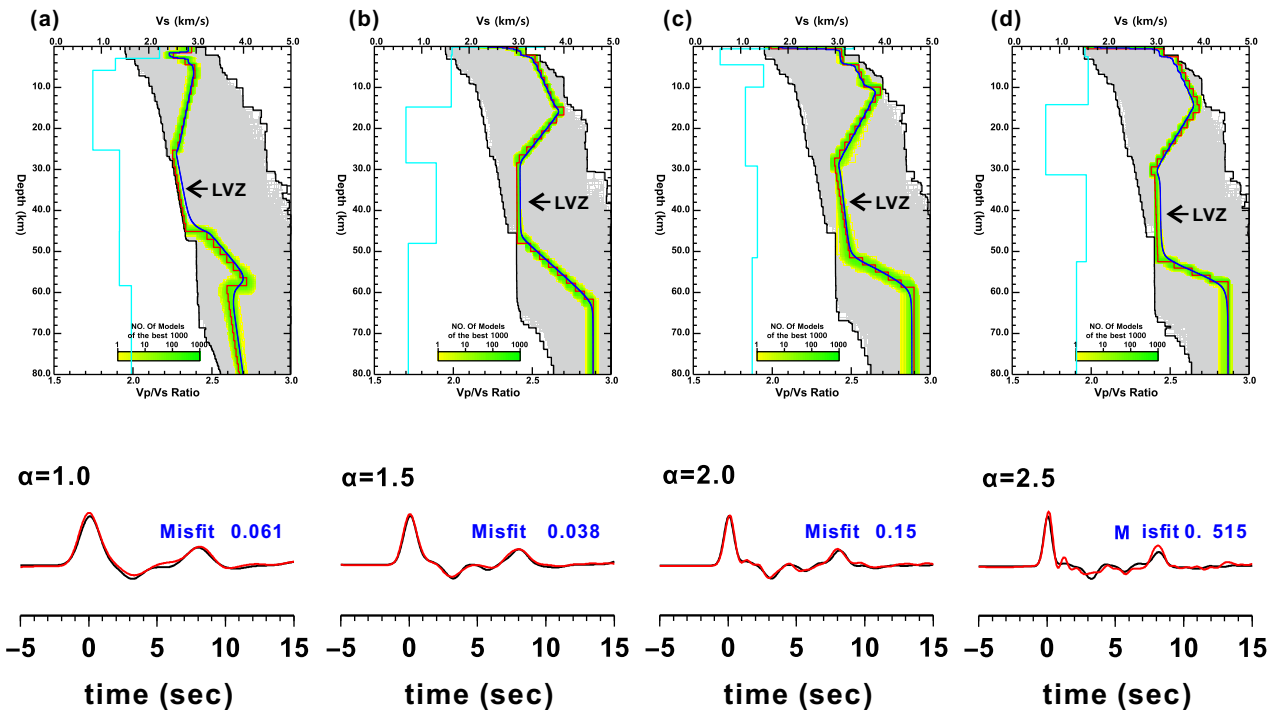


**Figure 5.** At station S16, results from receiver functions with different Gaussian parameter  $\alpha = 1.0, 1.5, 2.0$  and  $2.5$  are shown in the upper panels from left to right (a)–(d), respectively; below each of the four panel is the corresponding observed (black line) and synthetic (red line) receiver functions, while misfit value (blue) is also shown. The synthetics are based on the best-fitting model shown as the red line in the parameter space. Each panel on top contains defined model space (between two solid black lines), all generated models (grey lines), the best-fitting model (red line) and the average (blue line) of 1000 best-fitting models (shown in colour bar). The  $V_p/V_s$  ratio also is shown in cyan line corresponding to the best-fitting model.

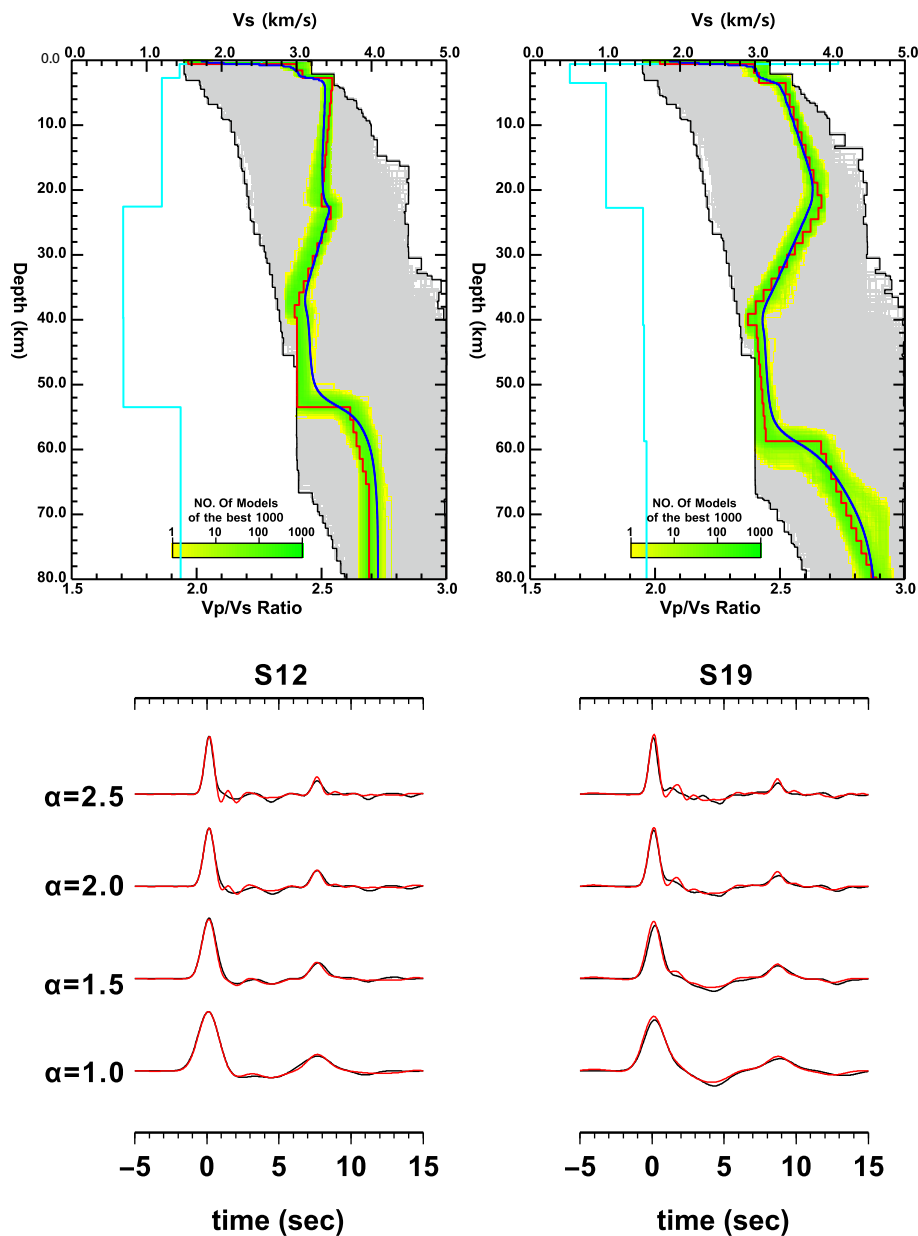


**Figure 6.** The comprehensive inversion results of NA method at station S12 (left) and S19 (right). See Fig. 5 for description. The lower panels show comparison between synthetics (red line) and observed (black line) receiver functions derived from four low-pass frequency Gaussian filters. The synthetics also are calculated based on the best-fitting model.

## 4 DISCUSSION

### 4.1 Low velocity zone near the surface

On account of complex tectonic settings in NE Tibet including a series of thrust and strike-slip faults, low shear wave velocity on the near surface at depth of 2–4 km shown in Fig. 10(c) may be attributed to tectonic destruction and unconsolidated sediments filled in the Cenozoic intramontane basins, such as Gonghe and Guide basins. The thickness of LVZ beneath Mado-Gande fault on the southern segment of the profile reaches about 10–15 km. This is probably influenced by the Middle to Late Triassic Songpan–Ganzi complex sediments with an estimated stratigraphic thickness of 10 km and locally reaching 15 km (Weislogel 2008). Meanwhile, the observed receiver functions of station S23 near Mado-Gande fault also show an obvious  $P$ -to- $S$  converted phase at time  $\sim 2.6$  s after the arrival of

direct  $P$  wave, which may be produced by the crystalized basement beneath the thickened sediments.

### 4.2 Low velocity zone in middle-to-lower crust

Variation of shear wave velocities along the profile is mostly prominent in the middle-to-lower crust. In the Songpan–Ganzi block, low shear wave velocity zone (LVZ) emerges at the depth of  $\sim 30$ –50 km; The LVZ extends further north to the southern margin of the Gonghe basin. Two previous joint-inversion results based on surface wave dispersions and receiver functions (Deng *et al.* 2015; Wu *et al.* 2017) also found the existing LVZ in the crust beneath Songpan–Ganzi block. Due to different methods and data set used, the depth ranges of the LVZ obtained from this study and the other

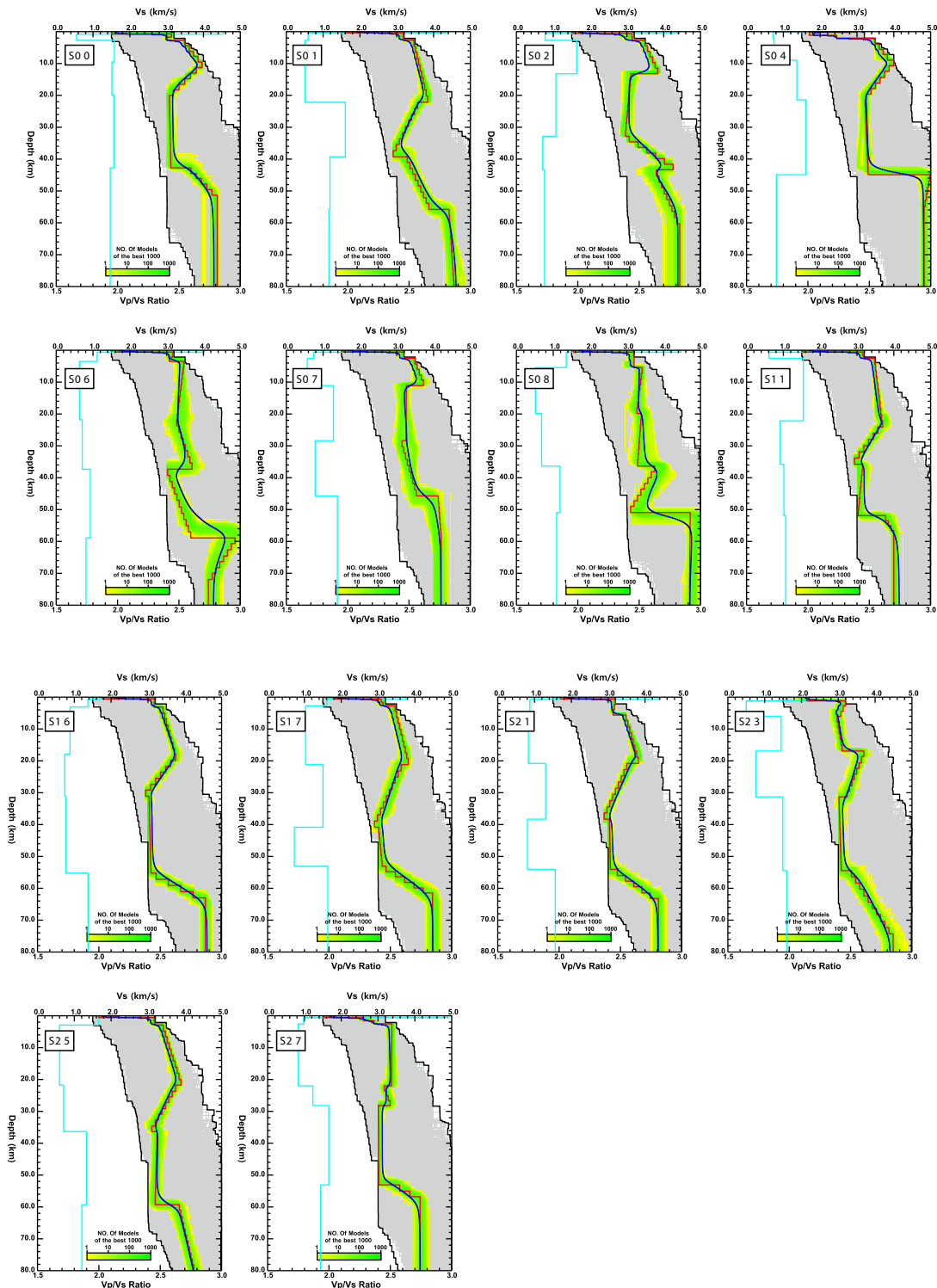
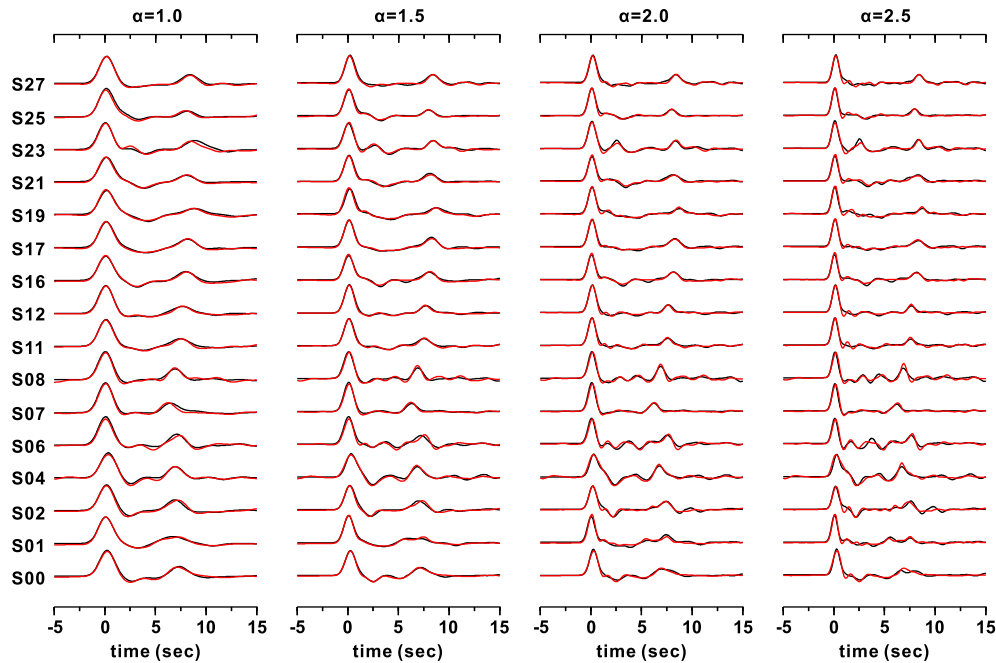


Figure 7. Similar with Fig. 5(a), but for comprehensive inversion results for the rest of 14 seismic stations.

two previous studies may be different, but they are generally in the depth of middle-to-lower crust.

The existences of LVZ in the NE Tibet have been reported in many studies, but distribution ranges are still controversial. The results of this study show that the LVZ is roughly confined to the Songpan–Ganzi block and Kunlun mountains and the southern margin of Gonghe basin. The observations from surface wave tomography already show prominent LVZ in middle-to-lower crust beneath the

Songpan–Ganzi block and the western part of Qilian block (Yang *et al.* 2012; Li *et al.* 2014a,b). In contrast, there is no obvious LVZ existing in the crust of Qaidam basin and Kunlun block. More complex behaviour of crustal deformation along the North Kunlun fault is depicted by Jiang *et al.* (2014). They constructed a 3-D crustal shear wave velocity model and found that the lateral distribution of LVZs exhibits significant west–east variations along this fault. In the west of 98° E, LVZs are confined to regions of the North



**Figure 8.** The comparison between the synthetics based on the best-fitting velocity model and the observations. The red lines represent synthetics and black lines represent observations. The left words represent the station name, respectively.

Kunlun fault and the eastern Ranges, while in the east of  $98^\circ$  E, LVZs extend and penetrate northward into the east Kunlun and Qinling Orogen over  $\sim 100$  km across the North Kunlun fault. Similar phenomenon is revealed by the recent study of teleseismic Rayleigh wave tomography in the NE Tibet. The researcher points out not only low velocities are characteristic in middle-to-lower crust of the Songpan–Ganzi block and West Qinling Orogen, but also the uppermost mantle of the Songpan–Ganzi block and the West Qinling Orogen is also characterized by an LVZ (Wei *et al.* 2017).

#### 4.3 Low velocity zone beneath the Songpan–Ganzi block

Generally speaking, three factors may attribute to the low velocities in Tibetan crust: high temperature, the appearance of fluid or partial melting and strong radial anisotropy. In fact, the mechanism that causes LVZ in middle-to-lower crust beneath the Songpan–Ganzi block has been in hot debate in many studies. Fig. 10 shows two  $P$ -wave velocity–depth profiles (Fig. 10a) located in the vicinity of Mado-Gande fault and North Kunlun fault, average crustal  $V_p/V_s$  ratio (Fig. 10b) and the comprehensive inversion result (Fig. 10c) in this study. The  $P$ -wave velocity structure is provided by wide-angle reflection–refraction seismic experiment (Zhang *et al.* 2011) along a very similar profile. The average  $V_p/V_s$  ratio in the crust is provided by  $H$ – $\kappa$  grid searching of receiver functions in this profile (Xu *et al.* 2014). Fig. 10(a) shows the  $P$ -wave velocity gradient (curves A and B) agrees well with that of the average continental crust (curve E), but the absolute value is lower by  $0.5 \text{ km s}^{-1}$  than the continental average. Considering the Songpan–Ganzi block is covered by  $\sim 10$  km of Triassic flysch, and therefore moving the curves A and B up by 10 km, the deviation from typical crust is till c.  $0.25 \text{ km s}^{-1}$ . These  $P$ -wave crustal velocity values may suggest that the crust of Songpan–Ganzi block is more felsic than normal, or the crustal temperature beneath the southern segment of the profile is  $500^\circ\text{C}$  above typical continental geotherms (Christensen 1979). The former assumption requires low crustal  $V_p/V_s$  ratio and

it may be inconsistent with the prominent low shear wave velocity displayed in the inversion results. So, the latter assumption seems to be more reasonable to explain both the low  $S$  velocities and high crustal  $V_p/V_s$  ratios (Xu *et al.* 2014). The LVZ in middle-to-lower crust beneath the Songpan–Ganzi block may be attributed to the partial melting induced by high temperature.

GPS measurements of the strain-rate field (Zhang *et al.* 2004) have revealed material is moving northward in the western Tibet and progressively to the northeastward in central Tibet and generally eastwards in the NE Tibet. In particular, the strain rate becomes larger and points southeastwards in the SE Tibet. Geophysical studies using different investigation methods have found high electrical conductivity, high temperature and low seismic velocity zone in the middle-to-lower crust beneath the northern and eastern plateau (e.g. Yao *et al.* 2008; Zheng *et al.* 2010; Li *et al.* 2014a). Combining with surface topography in the surroundings of Tibet, the channel flow model is proposed by Clark & Royden (2000) and suggests that influx of crustal material from the central plateau through ductile channel flow in the deep crust. Recent study based on the joint inversion of surface wave dispersions and receiver functions implemented by Liu *et al.* (2014) suggests that both local crustal flow and deep faults in SE Tibet play roles in accommodating the eastward extension of the Tibetan Plateau. In the NE Tibet, particularly Songpan–Ganzi block, LVZ observed in middle-to-lower crust correlates with other anomalous observations, such as low  $P_n$  velocity, high  $Q$  attenuation, low surface wave velocity zone, strong shear wave anisotropy (Liang & Song 2006; Kind & Yuan 2010; Yang *et al.* 2012; Zhao *et al.* 2013; Li *et al.* 2014a,b). High electrical conductivity may indicate the appearance of fluid or partial melting (Unsworth *et al.* 2004; Pape *et al.* 2012). The recent study based on the inversion of surface wave dispersions also reveals an obvious middle-crustal LVZ and low velocity anomaly in the upper mantle beneath the Songpan–Ganzi block. The authors suggest that the middle-crustal LVZ is attributed to the presence of partial melting (Li *et al.* 2017b). In the neighbouring Qiangtang block, recent studies report that low velocities in middle-to-lower crust may be

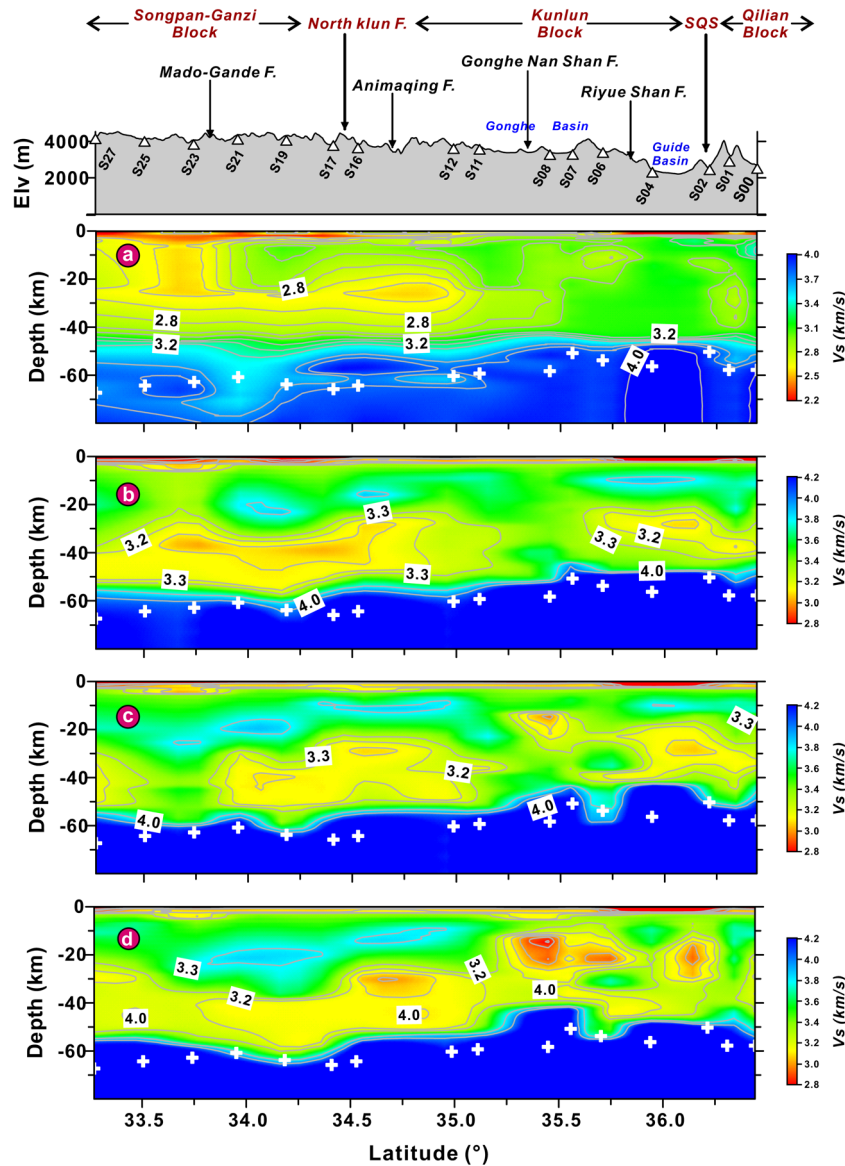


**Figure 9.** The top shows the surface topography, locations of 16 seismic stations and most of thrust and strike-slip faults in this profile. Gonghe and Guide basins are also shown. 2-D images of crustal shear wave velocity derived from different Gaussian parameters along the profile are shown as (Figs 9a–d). The Gaussian parameter  $\alpha$  for (a)–(d) are equal to 1.0, 1.5, 2.0 and 2.0, respectively. The white crosses represent averaged crustal thickness beneath seismic stations based on the H– $\kappa$  grid searching. Although there are some local differences between each other, an LVZ emerges undoubtedly in the middle-to-lower crust beneath the Songpan–Ganzi block, if only considering the velocity changes without regard of the absolute velocity value.

caused by partial melting and radial anisotropy of mica-bearing rocks with a subhorizontal dipping foliation (Hacker *et al.* 2014). In the Tibet, whatever mechanisms play a more important role in the formation of middle-to-lower crustal low velocities, the LVZ should have a great significance for investigating its dynamic evolution and laterally outgrowth mechanism.

## 5 CONCLUSIONS

Low shear wave velocity zone is found in the middle-to-lower crust of Songpan–Ganzi block beneath the profile. But it is roughly confined in the range of Kunlun mountains, and the southern margin of Gonghe basin. The crust of Songpan–Ganzi block also shows low  $P$ -wave velocities and high  $V_p/V_s$  ratio. These observations suggest that the LVZ may be attributed to partial melting induced by high temperature. This LVZ correlates with other anomalous obser-

vations in this region, such as low  $P_n$  velocity, high  $Q$  attenuation, low surface wave velocity zone, high electrical conductivity and strong shear wave anisotropy. The middle-to-lower LVZ beneath the Songpan–Ganzi block is similar to the LVZs observed beneath other parts of plateau, such as eastern, central and southeastern Tibetan Plateau. In the Tibet, whatever mechanisms play a more important role in the formation of middle-to-lower crustal low velocities, the LVZ should have a great significance for investigating its dynamic evolution and laterally outgrowth mechanism.

## ACKNOWLEDGEMENTS

We are thankful for Prof. Robert Herrmann, Saint Louis University, providing the computer software package to calculate the receiver functions and Prof. Sambridge, Australian National University, providing the NA method program. We gratefully acknowledge the

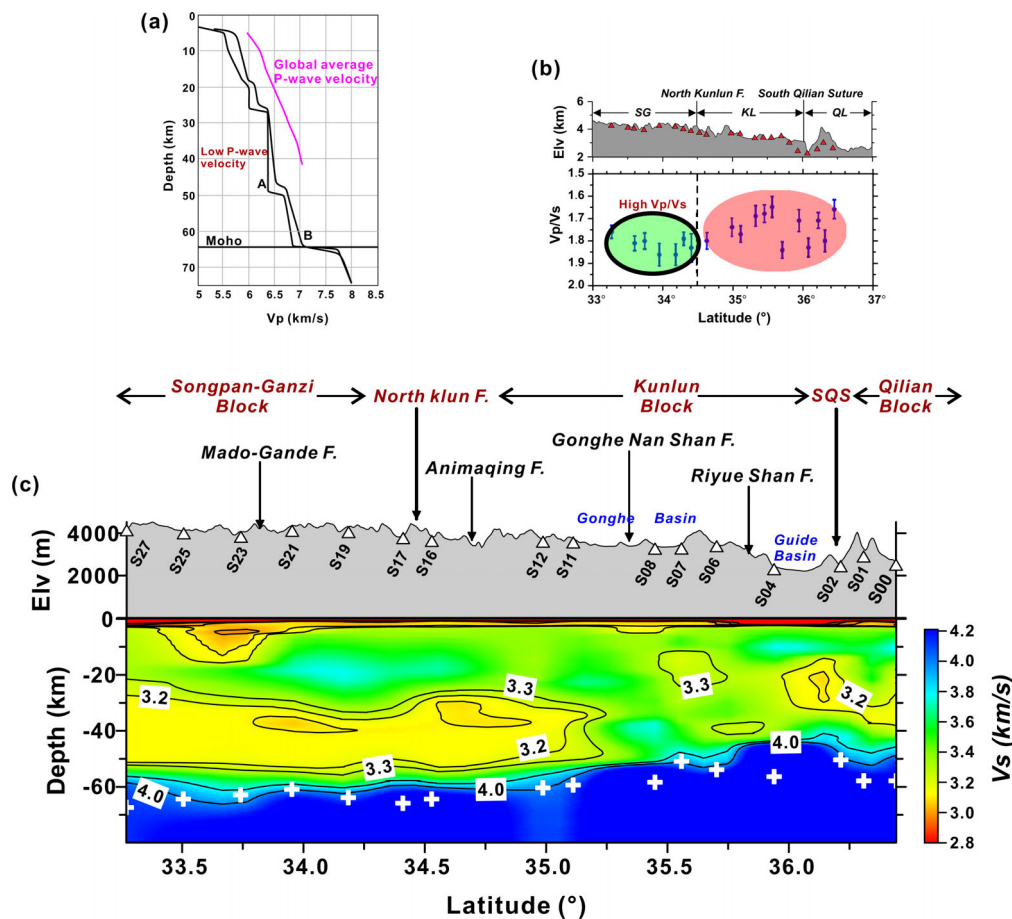


**Figure 10.** (a) Two  $P$ -wave velocity–depth profiles A and B located in the vicinity of Mado-Gande fault and North Kunlun fault, respectively, provided by the wide-angle reflection and refraction seismic experiment (Zhang *et al.* 2011). (b) The average ratio of  $V_p/V_s$  in the crust provided by the  $H$ - $\kappa$  method (Xu *et al.* 2014). (c) The crustal shear wave velocity structure along the profile derived from the comprehensive inversion results by simultaneously fitting four groups of receiver functions in the NA inversion for each station. The white crosses represent averaged crustal thickness beneath seismic stations based on the  $H$ - $\kappa$  grid searching. The top shows the surface topography, locations of 16 seismic stations, and most of thrust and strike-slip faults in this profile. Gonghe and Guide basins are also shown.

financial support for this work contributed by the National key research and development programme of China (2016YFC0600302) and the National Natural Science Foundation of China (41522401, 41474068 and 413401011).

## REFERENCES

- Bannister, S., Bryan, C.J. & Bibby, H.M., 2004. Shear wave velocity variation across the Taupo Volcanic Zone, New Zealand, from receiver function inversion, *Geophys. J. Int.*, **159**(1), 291–310.
- Christensen, N.I., 1979. Compressional wave velocities in rocks at high temperatures and pressures, critical thermal gradients, and crustal low-velocity zones, *J. geophys. Res.*, **84**(B12), 6849–6857.
- Clark, M.K. & Royden, L.H., 2000. Topographic ooze: building the eastern margin of Tibet by lower crustal flow, *Geology*, **28**(8), 703–706.
- Clark, M.K., Farley, K.A., Zheng, D.W., Wang, Z.C. & Duvall, A.R., 2010. Early Cenozoic faulting of the northern Tibetan Plateau margin from apatite (U-Th)/He ages, *Earth planet. Sci. Lett.*, **296**(1–2), 78–88.
- Deng, Y.F., Shen, W.S., Xu, T. & Ritzwoller, M.H., 2015. Crustal layering in northeastern Tibet: a case study based on joint inversion of receiver functions and surface wave dispersion, *Geophys. J. Int.*, **203**(1), 692–706.
- England, P. & Houseman, G., 1989. Extension during continental convergence, with application to the Tibetan Plateau, *J. geophys. Res.*, **94**(B12), 17 561–17 579.
- Enkelmann, E., Weislogel, A., Ratschbacher, L., Eide, E., Renno, A. & Wooden, J., 2007. How was the Triassic Songpan-Ganzi basin filled? A provenance study, *Tectonics*, **26**, TC4007, doi:10.1029/2006TC002078.
- Fang, X.M., Song, C.H., Dai, S., Zhu, Y.T., Gao, J.P. & Zhang, W.L., 2007. Cenozoic deformation and uplift of the NE Qinghai-Tibet Plateau: evidence from high-resolution magnetostratigraphy and basin evolution, *Earth Sci. Front.*, **14**(1), 230–242.
- Fu, B.H. & Awata, Y., 2007. Displacement and timing of left-lateral faulting in the Kunlun Fault Zone, northern Tibet, inferred from geologic and geomorphic features, *J. Asian Earth Sci.*, **29**(2–3), 253–265.
- Gan, W.J., Zhang, P.Z., Shen, Z.K., Niu, Z.J., Wang, M., Wan, Y.G., Zhou, D. & Cheng, J., 2007. Present-day crustal motion within the Tibetan plateau inferred from GPS measurements, *J. geophys. Res.*, **112**, B08416, doi:10.1029/2005JB004120.
- Galvé, A. *et al.*, 2002. Modes of raising northeastern Tibet probed by explosion seismology, *Earth planet. Sci. Lett.*, **203**(1), 35–43.
- Hacker, B.R., Ritzwoller, M.H. & Xie, J., 2014. Partially melted, mica-bearing crust in Central Tibet, *Tectonics*, **33**(7), doi:10.1002/2014TC003545.
- Hetényi, G., Rodolphe, C., Vergne, J. & Nábělek, J.L., 2006. The effective elastic thickness of the India Plate from receiver function imaging, gravity anomalies and thermomechanical modelling, *Geophys. J. Int.*, **167**(3), 1106–1118.
- Jiang, C.X., Yang, Y.J. & Zheng, Y., 2014. Penetration of mid-crustal low velocity zone across the Kunlun Fault in the NE Tibetan Plateau revealed by ambient noise tomography, *Earth planet. Sci. Lett.*, **406**, 81–92.

- Karplus, M.S., Klemperer, S.L., Lawrence, J.F., Zhao, W., Mechie, J., Tilmann, F., Sandvol, E. & Ni, J., 2013. Ambient-noise tomography of north Tibet limits geological terrane signature to upper-middle crust, *Geophys. Res. Lett.*, **40**(5), 808–813.
- Kind, R. & Yuan, X.H., 2010. Seismic images of the biggest crash on Earth, *Science*, **329**(5998), 1479–1480.
- Li, H.Y., Shen, Y., Huang, Z.X., Li, X.F., Gong, M., Shi, D.N., Sandvol, E. & Li, A.B., 2014a. The distribution of the mid-to-lower crustal low-velocity zone beneath the northeastern Tibetan Plateau revealed from ambient noise tomography, *J. geophys. Res.*, **119**(3), 1954–1970.
- Li, X.F., Li, H.Y., Shen, Y., Gong, M., Shi, D.N., Sandvol, E. & Li, A.B., 2014b. Crustal velocity structure of the northeastern Tibetan plateau from ambient noise surface-wave tomography and its tectonic implications, *Bull. seism. Soc. Am.*, **104**, doi:10.1785/0120130019.
- Li, Y.H., Wang, X.C., Zhang, R.Q., Wu, Q.J. & Ding, Z.F., 2017a. Crustal structure across the NE Tibetan Plateau and Ordos Block from the joint inversion of receiver functions and Rayleigh-wave dispersions, *Tectonophysics*, **705**, 33–41.
- Li, Y.H., Pan, J.T., Wu, Q.J. & Ding, Z.F., 2017b. Lithospheric structure beneath the northeastern Tibetan Plateau and the western Sino-Korea Craton revealed by Rayleigh wave tomography, *Geophys. J. Int.*, **210**(2), 570–584.
- Liang, C.T. & Song, X.D., 2006. A low velocity belt beneath northern and eastern Tibetan Plateau from Pn tomography, *Geophys. Res. Lett.*, **33**(22), L22306, doi:10.1029/2006GL027926.
- Liang, X.F., Sandvol, E., Chen, Y.J., Hearn, T., Ni, J., Klemperer, S., Shen, Y. & Tilmann, F., 2012. A complex Tibetan upper mantle: a fragmented Indian slab and no south-verging subduction of Eurasian lithosphere, *Earth planet. Sci. Lett.*, **333–334**, 101–111.
- Ligorria, J.P. & Ammon, C.J., 1999. Iterative deconvolution and receiver-function estimation, *Bull. seism. Soc. Am.*, **89**, 1395–1400.
- Liu, M.J., Mooney, W., Li, S.L., Okaya, N. & Detweiler, S., 2006. Crustal structure of the northeastern margin of the Tibetan plateau from the Songpan-Ganzi terrane to the Ordos basin, *Tectonophysics*, **420**(1–2), 253–266.
- Liu, Q.Y. *et al.*, 2014. Eastward expansion of the Tibetan Plateau by crustal flow and strain partitioning across faults, *Nature Geosci.*, **30**(5), 361–365.
- Meyer, B., Tapponnier, P., Bourjot, L., Métivier, F., Gaudemer, Y., Peltzer, G., Shunmin, G. & Zhitai, C., 1998. Crustal thickening in Gansu-Qinghai, lithospheric mantle subduction, and oblique, strike-slip controlled growth of the Tibet plateau, *Geophys. J. Int.*, **135**(1), 1–47.
- Mulch, A. & Chamberlain, C.P., 2006. The rise and growth of Tibet, *Nature*, **439**(7077), 670–671.
- Pan, S.Z. & Niu, F.L., 2011. Large contrasts in crustal structure and composition between the Ordos plateau and the NE Tibetan plateau from receiver function analysis, *Earth planet. Sci. Lett.*, **303**(3–4), 291–298.
- Pape, F.L., Jones, A.G., Vozar, J. & Wei, W.B., 2012. Penetration of crustal melt beyond the Kunlun Fault into northern Tibet, *Nature Geosci.*, **22**(5), 330–335.
- Royden, L.H., Burchfiel, B.C., King, R.W., Wang, E.C., Chen, Z.L., Shen, F. & Liu, Y.P., 1997. Surface deformation and lower crustal flow in Eastern Tibet, *Science*, **276**(5313), 788–790.
- Sambridge, M., 1998. Exploring multidimensional landscapes without a map, *Inverse Probl.*, **14**(3), 427–440.
- Sambridge, M., 1999. Geophysical inversion with a neighbourhood algorithm-I. Searching a parameter space, *Geophys. J. Int.*, **138**(2), 479–494.
- Sambridge, M., 1999. Geophysical inversion with a neighbourhood algorithm-II. Appraising the ensemble, *Geophys. J. Int.*, **138**(3), 727–746.
- Schimmel, M. & Paulssen, H., 1997. Noise reduction and detection of weak, coherent signals through phase-weighted stacks, *Geophys. J. Int.*, **130**(2), 497–505.
- Shen, X.Z., Yuan, X.H. & Liu, M., 2015. Is the Asian lithosphere underthrusting beneath northeastern Tibetan Plateau? Insights from seismic receiver functions, *Earth planet. Sci. Lett.*, **428**, 172–180.
- Sherrington, H.F. & George, Z., 2004. Crustal fabric in the Tibetan Plateau based on waveform inversions for seismic anisotropy parameters, *J. geophys. Res.*, **109**, B02312, doi:10.1029/2002JB002345.
- Snoke, J.A. & Sambridge, M., 2002. Constraints on the S wave velocity structure in a continental shield from surface wave data: comparing linearized least squares inversion and the direct search Neighbourhood Algorithm, *J. geophys. Res.*, **107**(B5), doi:10.1029/20001JB000498.
- Tapponnier, P. & Molnar, P., 1976. Slip-line field theory and large-scale continental tectonics, *Nature*, **264**(5584), 319–324.
- Unsworth, M. *et al.*, 2004. Crustal and upper mantle structure of northern Tibet imaged with magnetotelluric data, *J. geophys. Res.*, **109**(B2), B02403, doi:10.1029/2002JB002305.
- Vergne, J., Wittlinger, G., Hui, Q., Tapponnier, P., Poupinet, G., Mei, J., Herquel, G. & Paul, A., 2002. Seismic evidence for stepwise thickening of the crust across the NE Tibetan plateau, *Earth planet. Sci. Lett.*, **203**(1), 25–33.
- Wang, W.L., Wu, J.P., Fang, L.H., Lai, G.J. & Cai, Y., 2017. Sedimentary and crustal thicknesses and Poisson's ratios for the NE Tibetan Plateau and its adjacent regions based on dense seismic arrays, *Earth planet. Sci. Lett.*, **462**, 76–85.
- Wei, X.Z., Jiang, M.M., Liang, X.F., Chen, L. & Ai, Y.S., 2017. Limited southward underthrusting of the Asian lithosphere and material extrusion beneath the northeastern margin of Tibet, inferred from teleseismic Rayleigh wave tomography, *J. geophys. Res.*, **122**, 7172–7189.
- Weislogel, A.L., 2008. Tectonostratigraphic and geochronologic constraints on evolution of the northeast Paleotethys from the Songpan-Ganzi Complex, central China, *Tectonophysics*, **451**(1–4), 331–345.
- Wu, Z.B., Xu, T., Badal, J., Yao, H.J., Wu, C.L. & Teng, J.W., 2017. Crustal shear-wave velocity structure of northeastern Tibet revealed by ambient seismic noise and receiver functions, *Gondwana Res.*, **41**, 400–410.
- Xu, T., Wu, Z.B., Zhang, Z.J., Tian, X.B., Deng, Y.F., Wu, C.L. & Teng, J.W., 2014. Crustal structure across the Kunlun fault from passive source seismic profiling in East Tibet, *Tectonophysics*, **627**, 98–107.
- Yao, H.J., Beghein, C. & van der Hilst, R.D., 2008. Surface wave array tomography in SE Tibet from ambient seismic noise and two-station analysis—II. Crustal and upper-mantle structure, *Geophys. J. Int.*, **173**(1), 205–219.
- Yao, H.J., van der Hilst, R.D. & Montagner, J.-P., 2010. Heterogeneity and anisotropy of the lithosphere of SE Tibet from surface wave array tomography, *J. geophys. Res.*, **115**(B12), B12307, doi:10.1029/2009JB007142.
- Yang, Y.J., Ritzwoller, M.H., Zheng, Y., Shen, W.S., Levshin, A.L. & Xie, Z.J., 2012. A synoptic view of the distribution and connectivity of the mid-crustal low velocity zone beneath Tibet, *J. geophys. Res.*, **117**(B4), B04303, doi:10.1029/2011JB008810.
- Yin, A. & Harrison, T.M., 2000. Geologic evolution of the Himalayan-Tibetan orogen, *Annu. Rev. Earth planet. Sci.*, **28**(1), 211–280.
- Yuan, D.Y., Champagnac, J.D., Ge, W.P., Molnar, P., Zhang, P.Z., Zheng, W.J., Zhang, H.P. & Liu, X.W., 2011. Late Quaternary right-lateral slip rates of faults adjacent to the lake Qinghai, northeastern margin of the Tibetan Plateau, *Bull. geol. Soc. Am.*, **123**(9–10), 2016–2030.
- Zhang, P.Z. *et al.*, 2004. Continuous deformation of the Tibetan Plateau from global positioning system data, *Geology*, **32**(9), 809–812.
- Zhang, P.Z., Zheng, D.W., Yin, G.M., Yuan, D.Y., Zhang, G.L., Li, C.Y. & Wang, Z.C., 2006. Discussion on late Cenozoic growth and rise of northeastern margin of the Tibetan Plateau, *Quat. Sci.*, **26**(1), 5–13.
- Zhang, Z.J., Klemperer, S., Bai, Z.M., Chen, Y. & Teng, J.W., 2011. Crustal structure of the Paleozoic Kunlun orogeny from an active-source seismic profile between Moba and Guide in East Tibet, China, *Gondwana Res.*, **19**, 994–1007.
- Zhao, L.F., Xie, X.B., He, J.K., Tian, X.B. & Yao, Z.X., 2013. Crustal flow pattern beneath the Tibetan Plateau constrained by regional Lg-wave Q tomography, *Earth planet. Sci. Lett.*, **383**, 113–122.
- Zheng, D.W. *et al.*, 2006. Rapid exhumation at ~8 Ma on the Liupan Shan thrust fault from apatite fission-track thermochronology: implications for growth of the northeastern Tibetan Plateau margin, *Earth planet. Sci. Lett.*, **248**, 198–208.
- Zheng, Y., Yang, Y.J., Ritzwoller, M.H., Zheng, X.F., Xiong, X. & Li, Z.N., 2010. Crustal structure of the northeastern Tibetan plateau, the Ordos block and the Sichuan basin from ambient noise tomography, *Earthq. Sci.*, **23**, 465–476.